# Off-Design Performance of Molten Salt-Driven Rankine Cycles and its Impact on the Optimal Dispatch of Concentrating Solar Power Systems

William T. Hamilton<sup>a</sup>, Alexandra M. Newman<sup>a</sup>, Michael J. Wagner<sup>b</sup>, Robert J. Braun<sup>a,\*</sup>

#### Abstract

This paper presents a model for improving off-design performance predictions for molten salt-driven Rankine power cycles, such as in concentrating solar power tower applications. The model predicts cycle off-design performance under various boundary conditions, including molten salt inlet temperature, mass flow rate, and ambient temperature. The model is validated using industry performance data and benchmarked with results from the literature. A complete concentrating solar power plant, inclusive of solar heliostat field and receiver, is then considered, by implementing the Rankine cycle off-design performance results into the National Renewable Energy Laboratory's System Advisor Model software, which includes a tool that determines optimal power production schedules. The work improves upon the current System Advisor Model by updating off-design performance characteristics. A case study demonstrates the impact of cycle off-design behavior on annual performance for a stand-alone concentrating solar power system and a concentrating solar power-photovoltaic hybrid system. In addition, we demonstrate how cycle off-design performance influences optimal operator dispatch decisions and, thereby, overall system design and economics. We conclude that off-design cycle performance impacts "optimal" sub-system sizing, especially for a concentrating solar power-photovoltaic hybrid configuration in which concentrating solar power must dispatch in conjunction with photovoltaic generation.

Keywords: Off-design performance, Steam Rankine cycle, Concentrating solar power (CSP), Dispatch optimization, CSP-PV hybrid systems, Thermal energy storage (TES)

Preprint submitted to Energy Conversion and Management

September 17, 2020

<sup>&</sup>lt;sup>a</sup> Colorado School of Mines, Department of Mechanical Engineering, 1500 Illinois St., Golden, CO 80401, United States

<sup>&</sup>lt;sup>b</sup> National Renewable Energy Laboratory, Thermal Systems Group, 15013 Denver West Parkway, Golden, CO 80401, United States

<sup>\*</sup>Corresponding author

Email addresses: whamilton@mines.edu (William T. Hamilton), anewman@mines.edu (Alexandra M. Newman), michael.wagner@nrel.gov (Michael J. Wagner), rbraun@mines.edu (Robert J. Braun)

URL: aes.mines.edu (William T. Hamilton), orwe.mines.edu (William T. Hamilton),
orwe.mines.edu (Alexandra M. Newman), nrel.gov (Michael J. Wagner), aes.mines.edu (Robert J. Braun)

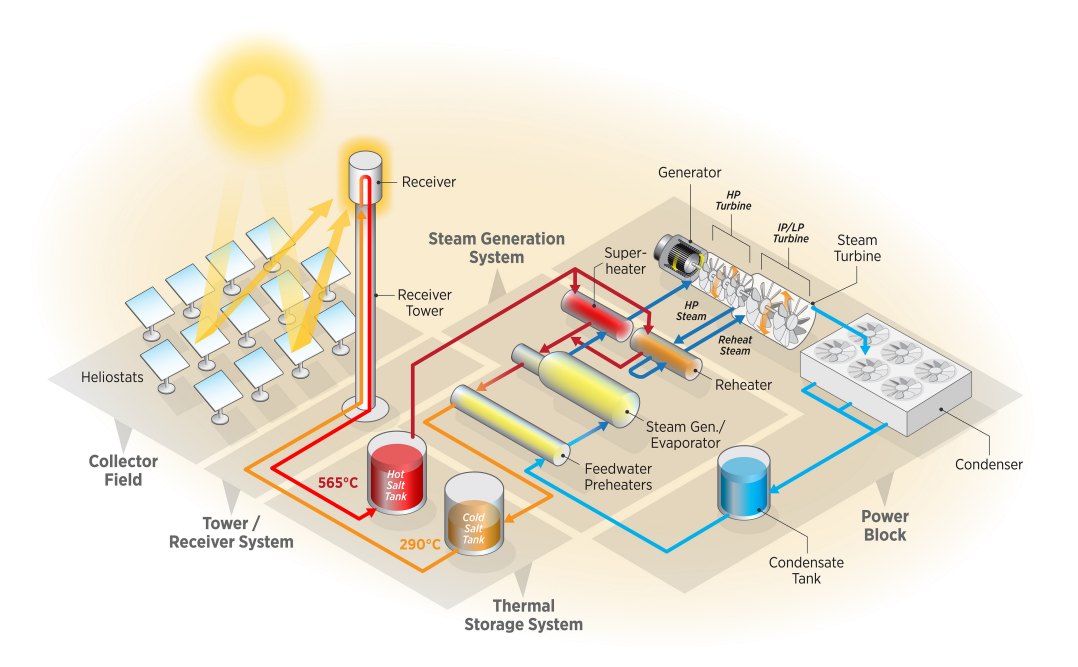


Figure 1: Molten salt power tower plant configuration. The system consists of a heliostat field, molten salt receiver, direct TES sub-system, a steam Rankine power generation cycle, and a heat rejection sub-system (Graphic © NREL/Al Hicks).

## 1. Background

Concentrating solar power (CSP) with thermal energy storage (TES) utilizes the solar thermal spectrum to generate, store, and dispatch heat to create on-demand electricity. Specifically, CSP power tower technology, depicted in Figure 1, consists of a field of heliostats that reflect sunlight to a central receiver where the flux concentration can be greater than 1,000 suns. Current utility-scale power tower systems employ liquid molten salt ( $60 \% \text{NaNO}_3 + 40 \% \text{KNO}_3$ ), operating between 290 °C and 565 °C, to transport thermal energy away from the receiver. The heated molten salt can either be immediately used to generate electricity via a Rankine power cycle, for example, or be stored in an insulated tank for use at a later time. When electricity generation is desired, high temperature molten salt flows through a series of heat exchangers where water is transformed into superheated steam that expands through a turbine, driving an electric generator. Examples of operational power tower CSP plants with TES include Gemasolar in Spain, Crescent Dunes in the United States, Noor III in Morocco, and Shouhang Dunhuang in China [1]. (Table 8 in the appendix provides a complete list of units, acronyms, model names, and notation.)

CSP systems with TES can dispatch renewable electricity to the grid when demand is the greatest. Due to TES, these systems have design flexibility that enables the decoupling of power output (power cycle rating) and energy capacity (hours of storage), but results in challenges when modeling system-level operations and annual performance. Specifically, CSP system generation is limited by its power cycle ramp rates due to

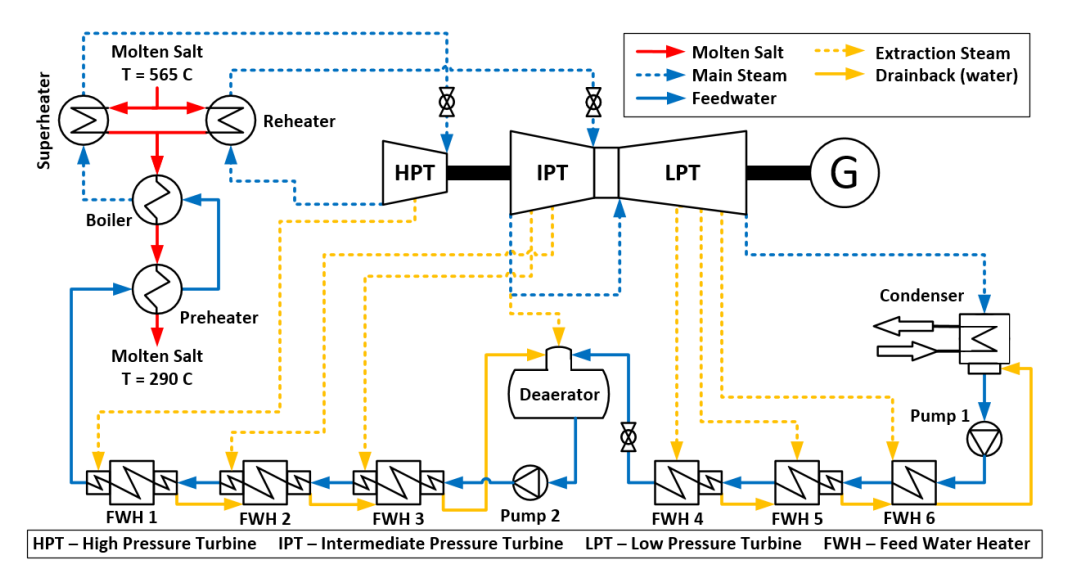


Figure 2: Molten salt-driven Rankine cycle with reheat, three turbine stages, and seven feedwater heaters, a sub-system in current commercial-scale CSP tower systems.

thermal gradients. Like traditional power systems, CSP Rankine cycle response time is a function of turbine temperature, which depends on the cooling rate and time since last operational. One of the greatest losses in the conversion of solar-to-electric energy results from the power cycle inefficiency at design and part-load conditions. Therefore, inability to accurately capture cycle efficiency leads to poor assessment of the value that a CSP system provides to the grid.

Figure 2 depicts a schematic of a prototypical power cycle in a CSP plant that employs a subcritical reheat regenerative Rankine cycle with seven feedwater heaters and a molten salt-to-steam heat exchanger train. Superheated steam leaving the salt-to-steam train expands through a high-pressure turbine (HPT), is reheated, and expands through the intermediate pressure turbine (IPT) and low pressure turbine (LPT), after which it is condensed into feedwater, and is pumped back to the salt-to-steam train. To improve efficiency, a small amount of steam is extracted at discrete locations during the turbine expansion to pre-heat the feedwater before the molten salt heat input. The individual components that constitute a Rankine cycle are sized to produce the highest efficiency when operating at design conditions, or design-point efficiency.

Balancing electricity supply to meet demand becomes an ever-increasing challenge as penetration levels of intermittent renewable energy, such as wind and solar, increase. To achieve high renewable-energy grid penetration requires either: (i) over-generation and, consequently, curtailment, (ii) integration of highly flexible generators, or (iii) adoption of energy storage technologies [2]. The objectives of our work are to: (i) understand molten salt-driven Rankine cycle performance for the two primary control strategies, (ii) evaluate optimal operational interactions between the Rankine cycle and solar collection under varying off-design performance assumptions, and (iii) explore and quantify off-design cycle performance impact on CSP power tower system design.

## 1.1. Rankine cycle part-load operation

CSP with TES systems are capable of producing electrical energy at a rate that is only loosely coupled with the solar energy collection process. Several factors can influence the selected power generation level, including TES state of charge, anticipated solar collection, power cycle startup and ramping specifications, and external factors such as current electricity market price. Furthermore, power cycle performance is altered as operating conditions deviate from their design-point values. Cycle thermodynamic efficiency, for example, is significantly reduced under part-load mass flow and/or reduced hot-side temperature conditions, or during elevated ambient temperatures. When conditions simultaneously depart from design, cycle performance cannot be expressed as a sum of independent effects; rather, detailed first-principles thermodynamics models are required to predict cycle performance, which is particularly important for CSP, where off-design operation can represent a significant fraction of operating hours.

In molten salt-driven Rankine cycles, one means by which electric power output can be reduced is by decreasing the salt mass flow rate, thereby reducing cycle heat input and the rate of steam generation in the salt-to-steam heat exchanger train. When steam mass flow rate is reduced and the turbine maintains fixed shaft speed, the turbine inlet pressure tends to decrease (resulting in a reduction of available energy in the steam turbines). Two options are available for managing boiler pressure under these conditions: the cycle's pumps can either (i) produce feedwater at the reduced pressure, or (ii) produce full-pressure feedwater in conjunction with a throttling valve at the turbine inlet. These two methods are referred to as sliding and constant pressure operations, respectively.

The advantage of the constant pressure operation is that the boiler does not experience pressure changes during part-load operation, which can reduce transient stresses during load changes; however, work is lost due the throttling process in the turbine control valves. Under sliding pressure operation, boiler pressure varies depending on cycle load; consequently, turbine control valves remain fully open, regardless of part-load operation, which mitigates irreversibilities from throttling. As the cycle power is reduced from design to part-load operations, the pressure rise requirements for the feedwater pumps are reduced and, consequently, pump work is decreased. Sliding pressure operation typically results in higher cycle thermal efficiencies at part-load than the constant pressure operation due to the reduced pump work and valve throttling irreversibilities. The main disadvantage of sliding pressure is a longer response time to load changes because the transients associated with boiler pressure are slower than the actuation of the control valves [3].

## 1.2. Related work

Overall cycle performance is primarily a function of individual component performance and cycle classification (sub-critical, supercritical, reheat, or regenerative). One of the largest uncertainties in predicting the part-load performance of steam turbines is properly evaluating the change in isentropic efficiency of the device. The standard methodology to model steam turbine off-design performance, in the absence of specific manufacturer test data, is the Spencer-Cotton-Cannon (SCC) method [4]. Spencer et al., which is a conservative approach in that actual turbine performance is approximately 2 % higher than calculated values predict [3].

The SCC method, in combination with Stodola's ellipse method [5, 6], has been used to model steam turbine performance with limited knowledge about turbine design

specifics. For example, Woudstra et al. [7] analyze the thermodynamic performance of a combined cycle utilizing Cycle-Temp, a power cycle modeling computer program which evaluates steam turbine performance. Chacartegui et al. [8] model and validate the performance of a 565 MW fossil fuel steam power plant to predict off-design performance of large steam turbines. For CSP applications, Marugán-Cruz et al. [9] conduct a parametric analysis of a direct steam generation linear Fresnel CSP plant. The authors implement turbine sliding pressure control and off-design cycle performance. McTigue et al. [10] model a double-flash geothermal power plant hybridized with a CSP field through the use of IPSEpro, employing Stodola's ellipse method to capture off-design behavior of the steam turbines. Brodrick et al. [11] use nonlinear optimization to determine an operational strategy for an integrated solar combined cycle and evaluate efficiency corrections for the steam turbine during part-load operations under varying solar resource and electricity prices. Based on literature, the SCC and Stodola's ellipse methods are implemented to model off-design turbine performance.

Researchers have developed models to determine optimal scheduling of system operations with and without off-design performance. Castronuovo and Lopes [12] propose an optimization model discretized at hourly fidelity to determine the optimum daily operational decisions for a wind farm with pumped hydro storage. However, no off-design performance is considered within the optimization model. Bischi et al. [13] develop a mixed-integer linear program to make short-term decisions for the operations of a combined cooling, heat and power energy system. The authors convert nonlinear off-design performance curves to piece-wise linear approximations and compare solution quality for varying piece-wise intervals. However, this work lacks a comparison between operational decisions using different performance curves. Zhou et al. [14] investigate the impacts of component off-design performance on the optimal design of combined cooling, heating, and power systems. The authors develop two optimization models that determine the design and operation of a combined cooling, heating, and power system: (i) assuming constant efficiency and (ii) considering equipment off-design performance. Their results indicate, for the given case study, that assuming constant efficiency provides a solution within 5% of a model that considers off-design performance. However, the system design is composed of discrete decisions regarding the number of a single type of equipment to acquire, which limits the design space.

Based on the literature, there exist methodologies to model Rankine cycle off-design performance; however, the impact of off-design performance on dispatch scheduling and design configuration of a CSP system is not well known. The primary contribution of our work lies in investigating and understanding the Rankine cycle off-design performance impact on optimized dispatch decisions and the propagation of those decisions into a CSP system's design, annual performance, and economics.

# 1.3. Overview of Paper

We develop and validate a Rankine cycle model with which to evaluate off-design performance and implement this model into existing simulation software – System Advisor Model (SAM)[15], which assesses renewable energy system performance and financial feasibility (see Figure 3). Section 2 describes in greater detail both SAM and the development of our Rankine cycle off-design performance model within Engineering Equation Solver. In addition, Section 2 includes a comparison of our Rankine cycle model's results against those derived from data obtained from a (confidential) industry partner and

from another model presented in literature. Section 3 describes the integration of our validated performance Rankine cycle model into SAM, provides a short description of our dispatch optimization methodology, and outlines a case study, which examines the impact of cycle off-design performance on optimal dispatch and its influence on system design, performance, and economics. Section 4 presents a comparison between our Rankine cycle model's off-design performance and SAM's default cycle. In addition, Section 4 discusses the impact of cycle off-design performance on optimal operations, annual metrics, and CSP system design. Section 5 concludes this paper with a summary of our findings.

## 2. Rankine Cycle Off-design Performance Models

One standard approach for evaluating the performance of thermal-energy-to-electricity conversion of a power tower CSP system utilizes SAM's Rankine cycle model, which we term (R) [16], and employs user-defined, high-level parameters and predefined look-up tables to model off-design cycle performance efficiently (described in greater detail later). (R) achieves a significant improvement over previous methods by (i) allowing SAM users to quickly evaluate power tower CSP system designs utilizing a Rankine cycle for thermal-energy-to-electric conversion, (ii) providing users convenient options for modeling different turbine inlet pressure control methods and condenser types, and (iii) enabling complex system control that can utilize dispatch optimization to maximize system revenue over an immediate time horizon [17]. Figure 3 depicts the information flow in the molten salt power tower model within SAM.

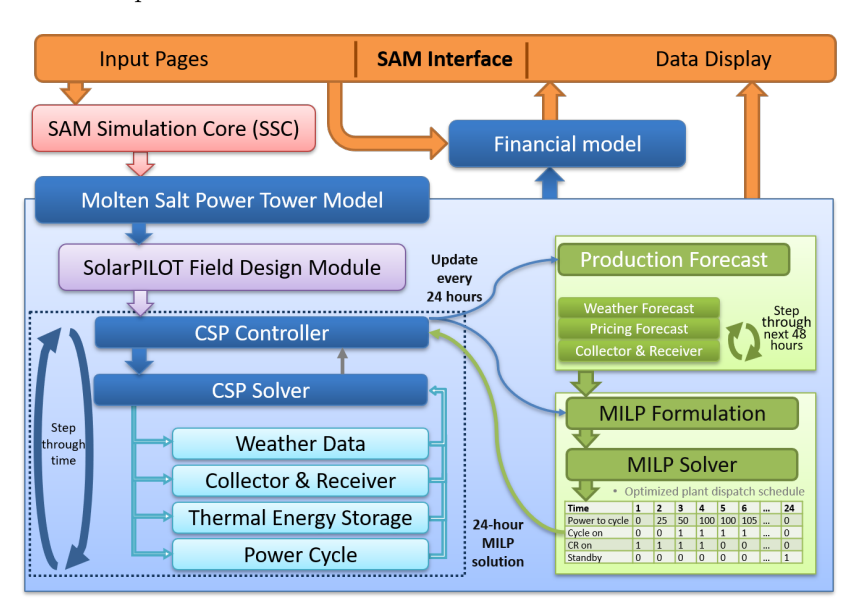


Figure 3: Information flow in the molten salt power tower model within SAM. The mixed-integer linear program (MILP) provides the hourly solution profile to the CSP controller, which sets target production levels and operational states for subsequent time horizons (figure modified from [17]).

SAM's Rankine performance model (R) employs a minimal set of user-defined cycle parameters to predict off-design cycle performance for an annual simulation, which includes options for turbine inlet pressure control, that is, fixed or sliding, and cycle condenser types, that is, evaporative, air-cooled, or hybrid. (R) utilizes a multiple-variable regression method to predict the cycle's electrical output for a given molten salt inlet temperature, molten salt mass flow rate, and condenser pressure. Molten salt inlet temperature and mass flow rate impact heat available to the cycle, while condenser pressure affects the available energy in the low pressure turbine's last stage.

An existing mixed-integer linear program interfaces with (R) to provide an optimal operating strategy by maximizing revenue over an immediate time horizon, subject to: (i) solar availability, (ii) electricity time-varying prices, (iii) operating costs, (iv) energy balances, (v) ramp rates, (vi) logical rules governing operations, and (vii) operational consistency between time periods [17, 18, 19]. When coupled with (R), this program can evaluate operational and design trade-offs for CSP and CSP-PV hybrid systems under various location and electricity market scenarios (see §3).

(R) estimates Rankine cycle performance given a cycle configuration and ambient conditions, but may be improved in several respects. Specifically, the relationship between heat input and electrical power output can overestimate cycle efficiency at part-load conditions (shown in §4.1). In commonly simulated plant configurations, the cycle often operates at or near design heat input. However, cycle part-load conditions occur more frequently when SAM is employed in conjunction with the dispatch optimization model [18], which can incorporate hybridization of CSP systems with photovoltaics [19].

## 2.1. Rankine Cycle Model Development

We develop a Rankine cycle model capable of off-design performance calculations using Engineering Equation Solver (EES) [20], referred to as (E), whose cycle configuration matches that of (R), as given in Figure 2, which depicts the modeled system containing steam reheat after expansion through the HPT and turbine extraction steam to one open and six closed feedwater heaters. In order to model the entry cycle at a fidelity capable of capturing off-design performance, each component design characteristic must be gathered either through literature, industry knowledge, or a design-point heat balance. To develop (E), we use a heat balance of a Rankine cycle rated at 125 MW $_e$  gross output provided by our industry partners. The heat balance contains pressures, temperatures, and mass flow rates before and after each component within the cycle at 100 % load condition and design ambient conditions.

## 2.1.1. Steam Turbines

Steam turbines convert fluid momentum into rotational energy, but this process is imperfect and thermodynamically irreversible and leads to exergetic (available energy) losses. The extent of these losses depends on the physical design of the turbomachinery and the fluid interaction with turbine blades, valves, housings, seals, and other turbine components. These effects can vary non-uniformly with operating conditions, including throttle steam temperature and pressure, rate of steam generation, and boiler saturation temperature. Given this complexity, predicting turbine thermodynamic efficiency is challenging even though it is one of the most significant aspects in capturing overall cycle performance under off-design conditions.

The SCC model was developed to predict turbine efficiency in a generalized manner, allowing for different turbine designs, operating conditions, and operating ranges by expressing performance according to normalized or nondimensionalized terms. The method specifies baseline efficiencies for various turbine sections and correction functions to account for volumetric flow rate, governing stage design, pressure ratio, initial conditions, partial throttle flow, and an optional mean-of-loops (a heat rate curve as a weighted average of the cycle performance over control valve actuations) [4]. In addition, the SCC method provides procedures for calculating packing leakages and turbine-generator losses associated with exhaust steam velocity, mechanical friction, and generator load.

For the development of (E), we model the HPT and the combined sections of the IPT and LPT using the SCC method described for a 3,600-rpm noncondensing one-row governing stage and a 3,600-rpm condensing without governing stage, respectively. We estimate values for a majority of the independent variables, that is, pressure ratios across stages, and steam flow rates at design, needed for the SCC method correction functions, using our industry partner's provided design-point heat balance. For the independent variables that cannot be estimated using heat balance information, we assume values based on engineering approximations and literature [3]. We assume that the HPT governing stage has four control valves and a pitch diameter of 38 inches (96.5 centimeters), a common configuration, along with an LPT last-stage annulus area of 55.6 square feet, i.e., 5.165 square meters, (afforded by a degree of freedom) because this area corresponds to performance closest to that predicted by our industry data when using the SCC method tabulated values of exhaust losses.

For part-load conditions, the HPT efficiency is primarily a function of the ratio between inlet flow rate at part load and the nominal design value. As this ratio decreases, the governing stage and overall HPT efficiencies decrease. On the other hand, the LPT efficiency is primarily a function of the annulus velocity of the last stage. We capture this effect using the SCC method through the calculation of exhaust losses, whose curves are a function of annulus velocity and are turbine-manufacturer-specific. However, the SCC method provides some representative relationships between annulus velocity and exhaust losses for various last-stage annulus areas.

During part-load conditions, extraction pressures, enthalpies, and mass flow rates vary as a function of throttle mass flow rate. To estimate extraction pressures and pressure after governing stage during part-load conditions, we implement Stodola's ellipse law [5], presented in Equation (1).

$$\frac{\dot{m}}{\dot{m}_{\rm D}} \frac{\sqrt{(P_{i,\rm D}P_{i,\rm D})^2}}{\sqrt{\rho_i P_i}} = \frac{\sqrt{1 - (P_o/P_i)^2}}{\sqrt{1 - (P_{o,\rm D}/P_{i,\rm D})^2}},\tag{1}$$

where  $\dot{m}$  is the mass flow rate through the turbine stage, P is pressure,  $\rho$  is density, the subscript i refers to stage inlet, the subscript o refers to stage outlet, and the subscript D refers to the design condition.

The SCC method provides turbine performance of the HPT and the combined sections of the IPT and LPT, which allows prediction of the outlet thermodynamic state of these two sections. Extraction enthalpies can be determined from an enthalpy-entropy (or Mollier) chart as the intersection of the extraction pressure and the turbine expansion curves, the former of which is provided by the Stodola's ellipse law and the latter of

which is approximated as follows: (i) for the HPT, as linear from the bowl condition (located between control valves and the first stage) to the turbine exit condition, and (ii) for the IPT and LPT, traditionally using a Keuffel and Esser curve number 1864-31 [4]; we develop a second-order polynomial using the heat balance information provided by our industry partners. The coefficient values of this polynomial function are proprietary information, but the general form is shown in Equation (2).

$$s(h) = a_0 + a_1 h + a_2 h^2 (2)$$

where s is entropy and h is enthalpy. For partial mass flow rates, expansion curves are offset relative to the design curves, intersecting the calculated end point [4]. An offset expansion curve is determined by offsetting the design curve by  $\Delta s$ , which is defined as the difference between turbine exit entropy at partial mass flow rate, s (determined by LPT exit pressure and enthalpy) and design entropy, s', given by Equation (2), using the turbine exit enthalpy (Equation (3)):

$$\Delta s = s(P_e, h_e) - s'(h_e) = s(P_e, h_e) - (a_0 + a_1 h_e + a_2 h_e^2)$$
(3)

where  $P_e$  is the LPT exit pressure and  $h_e$  is the LPT exit enthalpy. Equation (3) can be rewritten for extraction points, where entropy and enthalpy are unknown; see Equation (4)

$$s_e(h_e) = \Delta s + a_0 + a_1 h_e + a_2 h_e^2 \tag{4}$$

where  $s_e$  and  $h_e$  are the entropy and enthalpy, respectively, at IPT and LPT extraction points whose thermodynamic state can be fixed via Equation (4) in combination with an EES built-in entropy function using extraction enthalpy and pressure (the latter of which is determined by Stodola's ellipse law).

We estimate the turbine extraction mass flow by assuming a constant mass coefficient  $(\dot{m}/\sqrt{\rho P})$  for all partial flow rates, shown in Equation (5).

$$\frac{\dot{m}_e}{\dot{m}_{e,\mathrm{D}}} = \frac{\sqrt{\rho_e P_e}}{\sqrt{\rho_{e,\mathrm{D}} P_{e,\mathrm{D}}}},\tag{5}$$

where the subscript e refers to the conditions at turbine extraction.

## 2.1.2. Air-Cooled Condenser

Performance of the air- or water-cooled condenser dictates the relationship between condenser pressure, heat rejection, and ambient temperature. The condenser outlet is the lowest-energy state-point in the steam cycle, effectively setting a limit on the amount of available energy that the LPT can extract from the steam flow. Condenser pressure is a function of heat rejection load and ambient temperature, both of which routinely vary during off-design operation. Air-cooled condenser performance is manufacturer-specific and can be challenging to generalize. We employ air-cooled condenser data provided by our industry partner that expresses condenser pressure as a function of heat rejection load and ambient temperature. Because of the proprietary nature of the data, we normalize it using minimum condenser pressure, design heat rejection, and design ambient temperature (converted to Kelvin), shown in Figure 4 and explicitly denoted by markers.

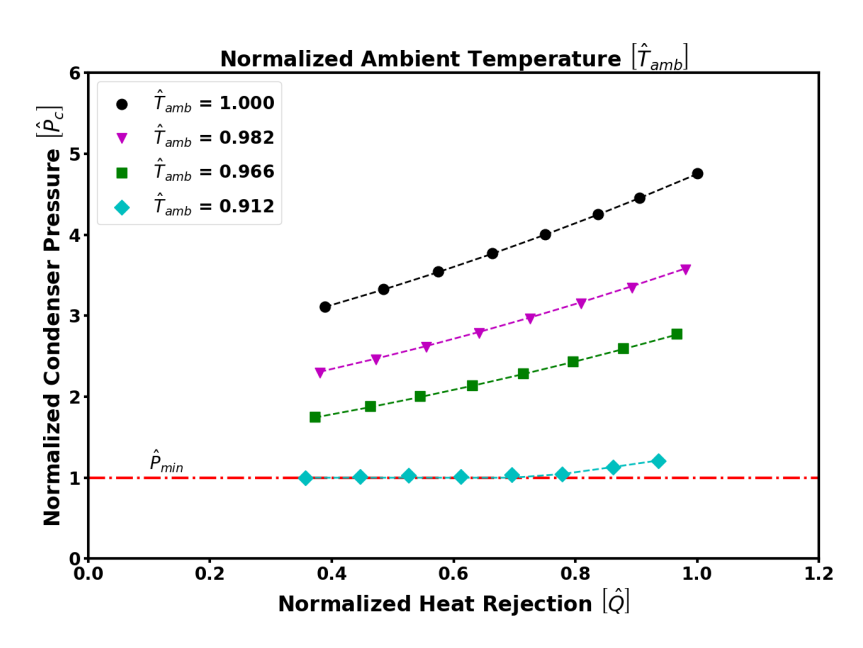


Figure 4: Normalized condenser pressure as a function of normalized heat rejection and normalized ambient temperature. Markers denote industry-provided data, while dashed lines depict the results from the fitted bi-variate polynomial (evaluated at the corresponding normalized ambient temperature and varying normalized heat rejection).

From this data, we develop a second-order bi-variate polynomial in terms of normalized ambient temperature,  $\hat{T}_{amb}$ , and normalized heat rejection,  $\hat{Q}$ , to determine normalized condenser pressure, shown in Equation (6):

$$\tilde{P}_c\left(\tilde{T}_{amb}, \hat{Q}\right) = \max\left\{\sum_{i \neq 0}^{2} \sum_{i=0}^{2} a_{ij} \hat{T}_{amb}^i \hat{Q}^j, 1.0\right\}$$

$$\tag{6}$$

where  $\tilde{P}_c$  is the normalized condenser pressure predicted by the bi-variate polynomial and  $a_{ij}$  is the coefficient for the (i,j) exponent pair (see Table 1).

Table 1: Fitted regression model coefficients for the corresponding (i, j) exponent pairs.

a			j	
a	ij	0	1	2
	0	147.966	71.235	27.554
i	1	-329.022	-159.268	-62.249
	2	183.460	89.502	35.571

When the bi-variate model predicts a normalized condenser pressure less than 1.0, for example, when  $\hat{T}_{amb} = 0.912$  and  $\hat{Q} \leq 0.7$  in Figure 4, the predicted value is set to 1.0 by the maximum function. By setting the predicted value to 1.0, condenser pressure is set to the minimum pressure for the condenser. With respect to the industry-provided data, our bi-variate polynomial has a root mean squared error of 0.0126, a mean absolute

error of 0.010, an R-squared value of 99.986 %, and an adjusted R-squared value of 99.982 %. Our bi-variate model is valid for conditions under which  $\hat{T}_{amb} \geq 0.8925$ ; for ambient temperatures below this condition, we assume that the air-cooled condenser performance does not change. We implement our bi-variate model into (E) to provide the relationship between ambient temperature, heat rejection, and condenser pressure.

To approximate condenser parasitic fan power, we assume a design approach temperature ( $\Delta T_{h,\mathrm{D}}$ ) of 3 °C, a design initial temperature difference (ITD<sub>D</sub>) of 16 °C, and constant specific heat of air ( $c_{air}$ ) evaluated at the design ambient temperature [21]. From these assumptions, we calculate design air mass flow rate ( $\dot{m}_{air,\mathrm{D}}$ ) to achieve the heat rejection load at design conditions ( $\dot{Q}_{rej,\mathrm{D}}$ ) using Equation (7).

$$\dot{m}_{air,D} = \frac{\dot{Q}_{rej,D}}{c_{air}(ITD_D - \Delta T_{h,D})}$$
 (7)

Next, we assume constant fan isentropic and mechanical efficiencies of 80 % and 94 %, respectively. In addition, we assume a pressure ratio across the fans to be constant at  $1.0028 \ (P_o/P_i)$  [21]. Assuming constant specific heat and ideal gas, temperature change for an isentropic process is defined by Equation (8).

$$T_{o,s} = T_i \left(\frac{P_o}{P_i}\right)^{R/c_{air}} \tag{8}$$

where  $T_i$  is fan inlet temperature (assumed to be ambient air temperature). With the approximate isentropic fan outlet air temperature known, fan outlet enthalpy can be calculated using the definition of isentropic efficiency for a fan. Fan power is estimated using Equation (9).

$$\dot{W}_{fan} = \frac{\dot{m}_{air} \left( h_o - h_i \right)}{\eta_{fan,m}} \tag{9}$$

where  $\eta_{fan,m}$  is the fan mechanical efficiency.

For part-load operation, we assume that the air-cooled condenser can only operate at discrete levels  $(n_{\rm acc,PL})$ , which could be the result of fan speed limitations (i.e., two- or three-speed fans) and/or the removal of condenser "bays" through system valving. For our purposes, we model these discrete levels by multiplying air mass flow rate at design conditions  $(m_{air,D})$  by a part-load fraction of the air-cooled condenser  $(f_{\rm acc,PL})$ .

We determine this part-load fraction by using Algorithm 1, which approximates condenser fan mass flow rate by assuming a constant approach temperature equal to design conditions. This algorithm decreases the condenser air flow rate when the predicted condenser pressure is greater than minimum pressure. The air mass flow rate returned by this algorithm impacts the condenser parasitic fan power, which influences net cycle efficiency.

#### 2.1.3. Feedwater Heaters and Pumps

To model the six closed feedwater heaters (shown in Figure 2), we assume that the design drain cooler temperature difference remains constant during off-design operation and neglect any heat losses to the surroundings. With these assumptions, the outlet condition of the extraction drain is known and feedwater outlet temperature can be determined

## Algorithm 1 Air-Cooled Condenser Part-load Air Mass Flow Rate

```
1: function ACC_PL_AIR(\dot{m}_{air,D}, \Delta T_{h,D}, P_{c,min}, T_{db}, n_{\text{acc,PL}}, Q_{rej})
         c_{air} := C_p(Air, T = T_{db})
                                                                                  ▷ Specific heat function call
 2:
         for i = 1, ..., n_{\text{acc,PL}} do
                                                                                              ▶ Turn off fan bays
 3:
              f_{\text{acc,PL}} := 1 - (i - 1)/n_{\text{acc,PL}}
                                                                                             \rhd \ {\bf Part\text{-}load} \ {\bf fraction}
 4:
 5:
              \dot{m}_{air} := \dot{m}_{air,D} \cdot f_{\text{acc,PL}}
                                                                       ▶ Mass flow rate through condenser
              \Delta T_{air} := \dot{Q}_{rej}/(\dot{m}_{air,D} \cdot c_{air})
                                                                       ▷ Estimate air temperature increase
 6:
              T_c := T_{db} + \Delta T_{h,D} + \Delta T_{air}
                                                                        ▶ Estimate condenser temperature
              P_c := P_{sat}(\text{Steam\_IAPWS}, T = T_c)
 8:
                                                                              ▶ Estimate saturation pressure
              if P_c > P_{c,min} then
 9:
                   Break
10:
              end if
11:
         end for
12:
         return \dot{m}_{air}
13:
                                                                                  ▶ Return air mass flow rate
14: end function
```

using an energy balance equation. Under normal operating conditions, feedwater heater performance has a small impact on overall cycle efficiency; however, removing a feedwater heater from service can impact cycle efficiency greatly [3].

Pressure drop through feedwater heaters is handled by Equation (10) [22]:

$$\Delta P = k\dot{m}^2,\tag{10}$$

where  $\Delta P$  is the difference between inlet and outlet pressures, k is a proportionality constant, and  $\dot{m}$  is the mass flow rate through the heat exchanger. For off-design conditions, we assume that the heat exchanger pressure drop varies with the square of mass flow rate.

To model the feedwater and boiler re-circulation pumps, we assume a design isentropic efficiency of 70 %. We adjust pump efficiency as a function of the ratio between part load and design mass flow rates using Equation (11) [22].

$$\frac{\eta_p}{\eta_{p,D}} = \beta + 2\left(1 - \beta\right) \frac{\dot{m}}{\dot{m}_D} - \left(1 - \beta\right) \left(\frac{\dot{m}}{\dot{m}_D}\right)^2,\tag{11}$$

where  $\eta_p$  is the pump isentropic efficiency,  $\beta$  is a shape factor parameter,  $\dot{m}$  is the mass flow rate, and the subscript D refers to design conditions. For (E), we assume that the shape factor parameter  $\beta$  is equal to zero.

## 2.1.4. Molten Salt-to-Steam Heat Exchangers

Figure 2 depicts the molten salt-to-steam heat exchanger train in the upper left. Commercial-scale projects have multiple, parallel trains to reduce the size of an individual heat exchanger, typically in the form of a counterflow shell-and-tube. The molten salt enters the salt-to-steam train at about 565 °C, where the flow is split into two, one directed to the superheater and the other directed to the reheater. This division of flow can either be constant or vary with cycle load. We utilize the former assuming the flow is split 50/50; the latter can be governed by the heat exchanger's thermal loads and an

Table 2: Design overall heat transfer coefficients  $(UA_D)$  and flow arrangements for the salt-to-steam heat exchangers within the steam generation system.

Heat Exchanger	$\mathrm{UA}_{\scriptscriptstyle \mathrm{D}} \left[\mathrm{kW/K} ight]$	Flow Arrangement
Preheater	2,672	Shell and Tube (One Shell Pass)
Boiler	5,270	Phase Change
Superheater	1,405	Counterflow
Reheater	667	Counterflow

equal exit temperature condition. After exiting the superheater and reheater, the two molten salt flows merge and progress through the boiler and preheater, where flow exits the steam generator at approximately 290 °C. At design conditions, the target turbine inlet temperature of both the HPT and IPT sections is 540 °C.

To model the salt-to-steam heat exchanger train, we utilize the effectiveness-NTU method to predict water and salt outlet temperatures at partial flow conditions [23]. Table 2 contains the design overall heat transfer coefficients  $(UA_D)$  and flow arrangements we implement to model the steam generation system. Heat loss to the surroundings is neglected for all heat exchangers in the salt-to-steam train. For partial flow conditions, we adjust the design overall heat transfer coefficients using Equation (12) [24].

$$\frac{\text{UA}}{\text{UA}_{\text{D}}} = \frac{\dot{m}_{h}^{0.8} \dot{m}_{c}^{0.8}}{\dot{m}_{h,\text{D}}^{0.8} \dot{m}_{c,\text{D}}^{0.8}} \frac{\dot{m}_{h,\text{D}}^{0.8} + \dot{m}_{c,\text{D}}^{0.8}}{\dot{m}_{h}^{0.8} + \dot{m}_{c}^{0.8}} \right)$$
(12)

where UA is the overall heat transfer coefficient,  $\dot{m}$  is mass flow rate, the subscripts h and c refer to the hot and cold side of the heat exchanger, respectively, and the subscript D refers to the nominal design value. We model pressure drop through the heat exchangers in the salt-to-steam train using Equation (10).

Using the effectiveness-NTU method, we solve for the exit temperatures of the molten salt and water for the preheater, superheater, and reheater. In addition to a shell-and-tube salt-to-steam heat exchanger, the boiler system consists of a steam drum and a re-circulation pump; this configuration ensures saturated vapor at the steam drum outlet for all partial flow conditions that we investigate. For the boiler system, we calculate the steam flow rate for the given feedwater inlet and outlet conditions, salt flow rate, and salt inlet temperature.

## 2.1.5. Sliding and Constant Pressure Operation

For both sliding and constant pressure operation, Equation (1) estimates "desired" steam pressure after the HPT governing stage, starting with the condenser pressure and working backwards through each turbine with respect to inlet pressure. For sliding pressure operation, boiler pressure is estimated using an assumed constant 4 % pressure drop across the HPT stop-and-control valves and the pressure drop through the superheater. As load decreases, boiler pressure decreases, which results in a decrease in molten salt preheater outlet temperature. If the boiler pressure continues to slide, the molten salt outlet temperature can start to crystallize (at 238 °C [25]). To address this, the boiler pressure is allowed to decrease to a point, after which it is held constant. We assume this point occurs at 80 bar, which is about 60 % power output.

For constant pressure operation, the boiler remains at a pressure of 125 bar and the steam is throttled to the "desired" steam pressure at the HPT governing stage outlet. Henceforth, we denote off-design performance cycle models (R) and (E) pertaining to sliding and constant boiler pressure operation, using superscripts s and c, respectively.

## 2.2. Validation and Error Analysis of model (E)

To validate (E), we compare relative heat rate,  $\overline{HR}$ , (for sliding pressure operation) predicted by (E<sup>s</sup>) against data provided by our industry partner, hereafter referred to as (D), for varying load fractions and normalized ambient temperatures (see Figure 5). Relative heat rate is defined as the ratio of heat rate at an off-design condition and design heat rate, which is equivalent to the ratio design gross cycle efficiency and off-design gross cycle efficiency (shown in Equation (13)); partial load fraction is defined as the ratio of cycle gross electric output at an off-design condition and the gross design electric output (shown in Equation (14)).

$$\overline{HR} = \frac{HR_{\rm PL}}{HR_{\rm D}} = \frac{\eta_{g,\rm D}}{\eta_{g,\rm PL}} \tag{13}$$

$$f_{\rm PL} = \frac{\dot{W}_{g,\rm PL}}{\dot{W}_{g,\rm D}} \tag{14}$$

In other words, a relative heat rate of 1.1 at a load fraction of 0.5 corresponds to the cycle requiring 10 % more heat per unit of power compared to design-point conditions, when producing 50 % of design output. Our analysis calculates relative heat rate using gross cycle efficiencies to effect results agnostic to the heat rejection system parasitic power requirements.

Figure 5 presents relative heat rate data (D) shown as symbols; predictions from  $(\mathsf{E}^s)$  for relative heat rate are represented by lines of the corresponding color.  $(\mathsf{E}^s)$  adequately predicts cycle performance for the range of load fraction and the various normalized ambient temperatures provided in the data. Figure 5 shows that, as ambient temperature decreases, relative heat rate at full load conditions (i.e., partial load fraction equal to 1) decreases, resulting in an increase in cycle efficiencies. Likewise, at ambient temperatures below design conditions, the part-load adverse effects, represented by the derivative of the curve, decrease, resulting in more favorable operation conditions at partial load fractions. However,  $(\mathsf{E}^s)$  systematically underpredicts relative heat rate at partial load fractions above 0.5 and overpredicts at low partial load fractions.

Figure 6 depicts the relative heat rate error, defined as (D) less (E<sup>s</sup>) (shown in Equation (15)), as a function of partial load fraction for various normalized ambient temperatures. The largest error is -0.0212 and occurs at low normalized ambient temperature (0.912) and low partial load fraction (0.3), which corresponds to a relative error of 2.08 %. With respect to (D), (E<sup>s</sup>) predicts relative heat rate with a root mean squared error of  $8.59 \times 10^{-3}$  and a mean absolute error of  $7.30 \times 10^{-3}$ . The error occurring at  $\hat{T}_{amb} = 1.0$  and  $f_{\rm PL} = 0.9$  appears to be the result of an outlier in the provided dataset (D) depicted in Figure 5. In summary, (E<sup>s</sup>) produces a small degree of error compared to (D) and appears to adequately represent off-design performance for a molten salt-driven Rankine

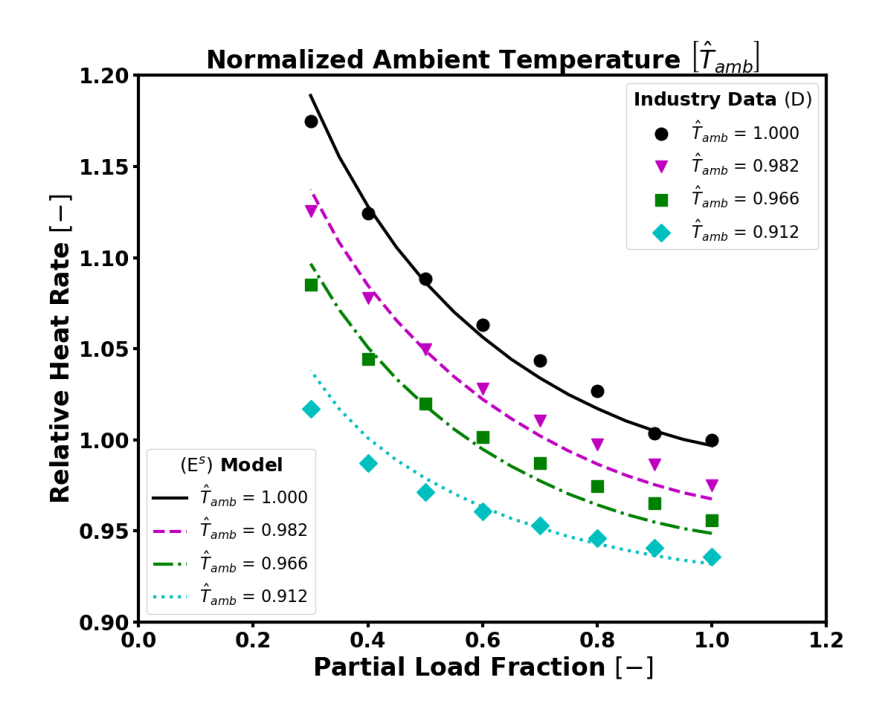


Figure 5: Relative heat rate (for sliding pressure operation) as a function of partial load fraction and various normalized ambient temperatures. Industry data (D) is represented by symbols and the prediction of the  $(E^s)$  model is represented by lines of the corresponding color.

cycle operating with sliding boiler pressure and using an air-cooled condenser for heat rejection.

Relative Heat Rate Error = 
$$\overline{HR}_{(D)} - \overline{HR}_{(E^s)}$$
 (15)

Lacking cycle performance data for constant pressure operation from our industry partners, to validate the cycle performance predictions for (E<sup>c</sup>), we compare its relative heat rate curve to that given by an open-source script that implements the SCC method in MATLAB<sup>®</sup> [26], shown in Figure 7. Utilizing the design heat balance, we provide Cicala's [26] model with the appropriate SCC method assumptions for our cycle configuration, that is, turbine type, pitch diameter, and LPT last-stage annulus area. For condenser pressure, we provide Cicala's model with predictions given by (E<sup>c</sup>) of condenser saturation temperatures for design and minimum throttle flow conditions, for which Cicala's model assumes a linear relationship under partial load.

Figure 7 demonstrates that the heat rate predicted by  $(E^c)$  is in close agreement with that predicted by Cicala's model. However, the prediction given by  $(E^c)$  deviates from those of Cicala's model conservatively at low partial load fractions. The two models' relative heat rate predictions are within 1 % of each other at our assumed lowest partial load fraction (30 % load). Based on this comparison, the estimate given by  $(E^c)$  for relative heat rate closely matches the results given by Cicala's model.

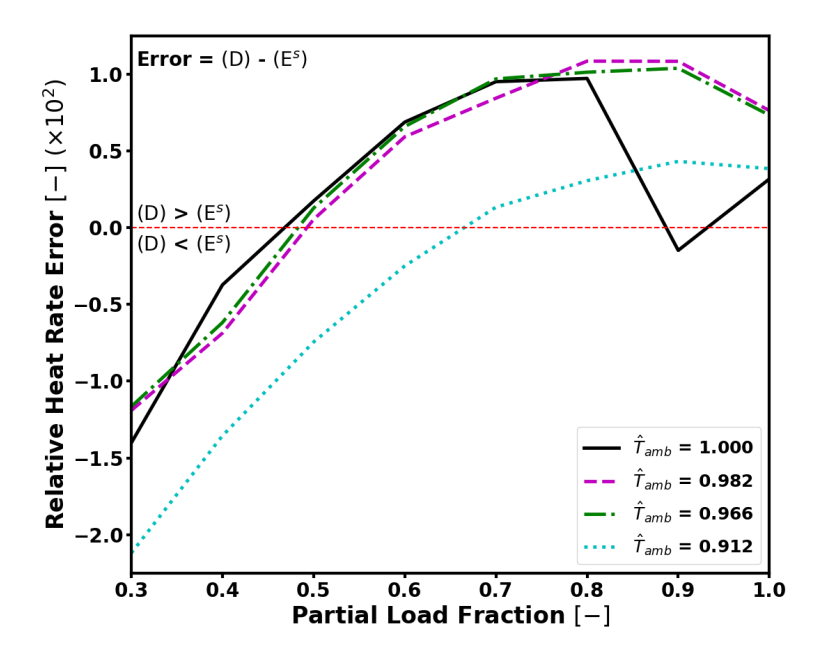


Figure 6: Relative heat rate error, defined as (D) less  $(\mathsf{E}^s)$ , as a function of partial load fraction for various normalized ambient temperatures.

## 2.3. Significance of Partial Load Efficiency

We demonstrate the significance of steam turbine and generator efficiency assumptions by comparing cycle relative heat rate curves under various assumptions and with different methods. Using  $(E^c)$ , we predict relative heat rate curves using: (i) the SCC method for both the turbine and generator efficiencies, (ii) constant turbine efficiency and using the SCC method for generator efficiency (losses), and (iii) constant turbine and generator efficiencies. For the constant efficiency cases, we calculate the HPT, IPT/LPT, and generator efficiencies for  $(E^c)$  using the SCC method, under fixed design flow and ambient temperature conditions, as 85.7 %, 89.7 %, and 98.3 %, respectively.

Figure 8 depicts the relative heat rate curves under various assumptions used to predict turbine and generator efficiencies at partial load. As expected, there is a significant deviation between relative heat rate curves using the SCC method and constant efficiency assumptions. The implications of this deviation could result in an under estimation of molten salt consumption as the Rankine cycle ramps to full load, which would result in less electricity generation, and correspondingly, less plant revenue.

## 3. Integration of (E) into SAM and Case Study

The *User Defined Power Cycle* option integrates the calculated cycle performance of (E) into SAM. For user-defined cycles, SAM employs a design-of-experiments technique to capture the main and interaction effects of molten salt mass flow rate, molten salt temperature, and ambient temperature on cycle thermal input, cycle gross electrical output, electrical power consumption for cooling, and cooling water flow rate. Implementation of

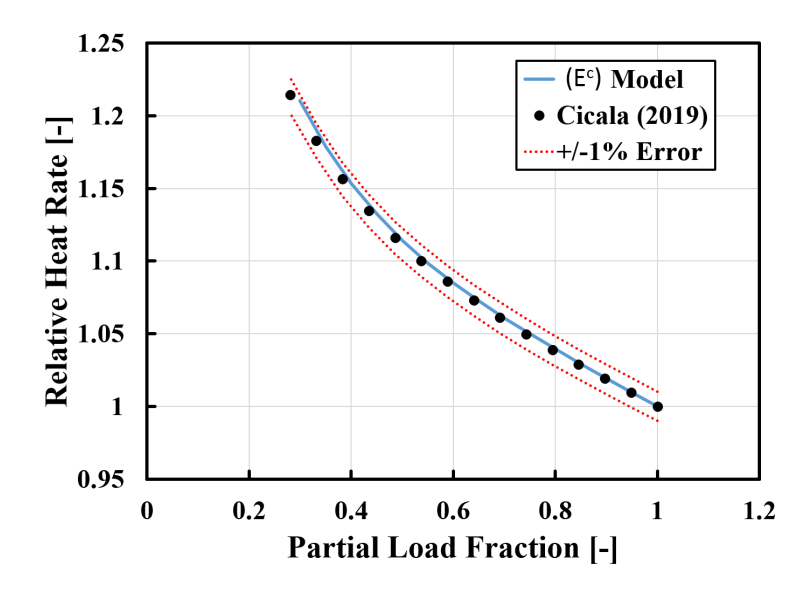


Figure 7: Comparison of Cicala's model and  $(E^c)$  predicted relative heat rates as a function of partial load fraction for constant boiler pressure operation at design ambient temperature.

Table 3: Low, design, and high parameter values used to generate cycle performance maps of (E) for SAM.

Parameter	Units	Low	Design	High
Molten Salt Temperature	°C	550	565	580
Normalized Molten Salt Mass Flow Rate	-	0.30	1.00	1.05
Ambient Temperature	$^{\circ}\mathrm{C}$	15	43	55

a user-defined cycle is described in detail within SAM's help documentation [27]. Table 3 presents low, design, and high parameter values used to generate cycle performance maps of (E) for SAM. Additionally, we assume that the air-cooled condenser system of (E) consumes 4.0 % gross power at design conditions.

## 3.1. Annual Simulations Utilizing Dispatch Optimization

To investigate the impact of off-design cycle performance on system economics, we employ work that integrates SAM's simulation core with dispatch optimization. Our software framework, shown in Figure 9, enables us to utilize dispatch optimization to evaluate the performance and economics of CSP-only, CSP-PV (photovoltaic) hybrids, and CSP-PV with battery storage designs. Our dispatch optimization model determines the operating schedule of each sub-system in the design to maximize revenue over the time horizon. Our annual simulation and dispatch optimization is capable of evaluating system performance at hourly and sub-hourly time fidelity. Wagner et al. [17] and Hamilton et al. [19] provide a detailed description of the software framework and a complete formulation of the dispatch optimization model.

Within our dispatch optimization model, we penalize system operations using estimated maintenance costs incurred from said operations. For the power cycle, the dispatch

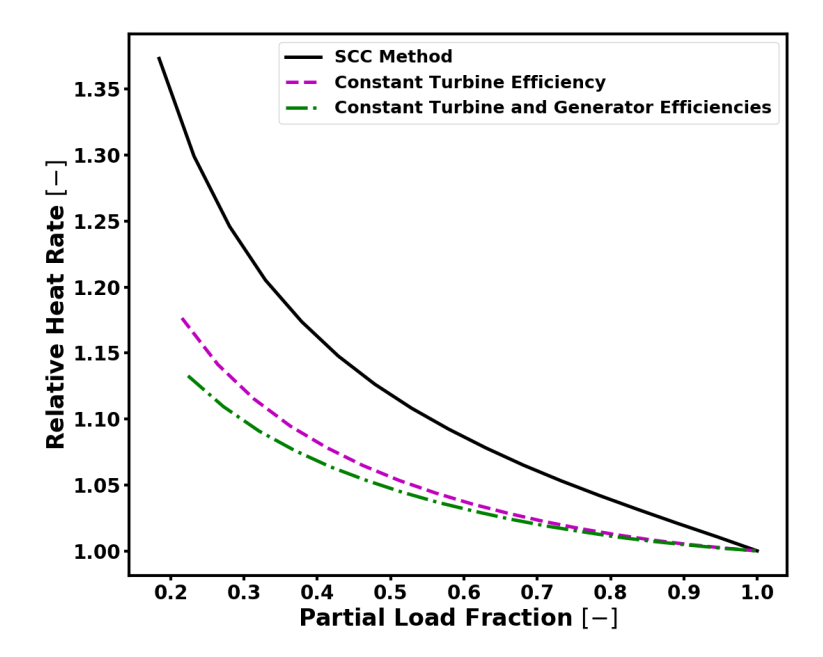


Figure 8: Cycle relative heat rate as a function of partial load fraction at design ambient temperature, under various assumptions used to predict turbine and generator efficiencies.

optimization model penalizes operating power output, changing power output between time periods (ramping), and starting the cycle from an off state. Due to the limited solar resource and depending on the design, CSP systems are unable to operate at full load through the night. Therefore, the tradeoff lies in (i) operating at partial load through the night at the cost of lower cycle efficiency and increased hours of operation, or (ii) operating at full load until thermal energy storage is depleted, shutting the cycle down, and starting up when solar resource is available. Power cycle part-load efficiency impacts this decision by dictating the solar-to-electric conversion, which directly influences the return on investment of the system.

#### 3.2. Case Study

This case study examines the impact of cycle off-design performance on optimal dispatch and its influence on system design, performance, and economics. We choose Rice, California, referred to hereafter as "Rice," and use the plant's location and typical meteorological year weather data at hourly time fidelity. This abandoned township has been explored as a potential location for a CSP system [18] because of suitable solar resource levels, proximity to grid transmission and interconnection points, and accessibility, among other factors. However, at the time of this writing, the authors are not aware of any active CSP project development at Rice.

To be consistent with the geographic location of Rice, we choose the Southern California Edison 2015 pricing schedule as the electricity market against which to dispatch power. This electricity market has hourly prices differentiated by weekday, weekend, and

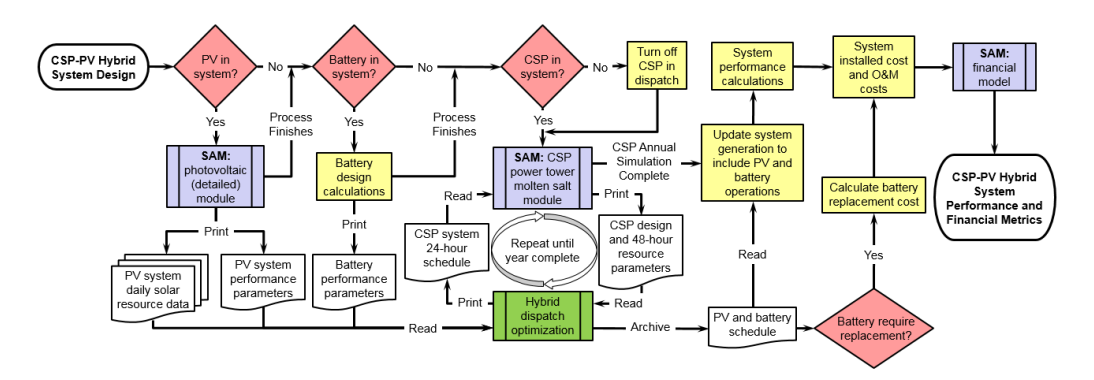


Figure 9: Flow diagram of the software architecture implemented around the hybrid dispatch optimization model.

Table 4: Low and high system design parameter values and the corresponding sampling interval used to generate a uniform mesh of system designs.

Design Parameter	Units	Low	High	Interval
Solar Multiple	-	0.50	3.50	0.25
Hours of Thermal Storage	Hours	4	16	2
PV Field Capacity	$\mathrm{MW}_{\mathrm{DC}}$	0	225	25
DC-to-AC Ratio	$\mathrm{MW}_{\mathrm{DC}}/\mathrm{MW}_{\mathrm{AC}}$	1.0	1.3	0.1

season, with the highest-value time periods occurring between the hours of 2 and 8 p.m. on weekdays during the months of June through September.

For the CSP system design, we utilize a 163 MW $_e$  gross output air-cooled Rankine cycle with a design ambient temperature of 43 °C, a gross cycle efficiency of 41.2 %, and the ability to operate between 30 and 105 % of partial load fraction, the latter of which is based on turbine vendor specifications for acceptable operating limits. To understand the impact of cycle performance on system design, we construct case studies by using a full-factorial design of experiments with the parameters listed in Table 4 between the low and high ranges at specified intervals; this results in 3,640 instances. Each design case is evaluated under the following assumptions: (i) the combined power output is grid-limited to 165 MW $_e$ , (ii) the PV sub-system possesses single-axis tracking with zero tilt, and (iii) the system contains no electric battery storage. Given the solar resource at Rice and the solar multiple, SolarPILOT [28] generates the CSP heliostat field layout and receiver design parameters, such as tower height, receiver height and diameter.

In addition to off-design performance cycle models (R) and (E), we include a constant efficiency model to which we refer as (C). We assume that (C) operates at design-point efficiency for all combinations of partial loads and ambient temperature conditions. We compare the behavior of (R) and (E) to that of the baseline case with no cycle efficiency degradation, given by (C).

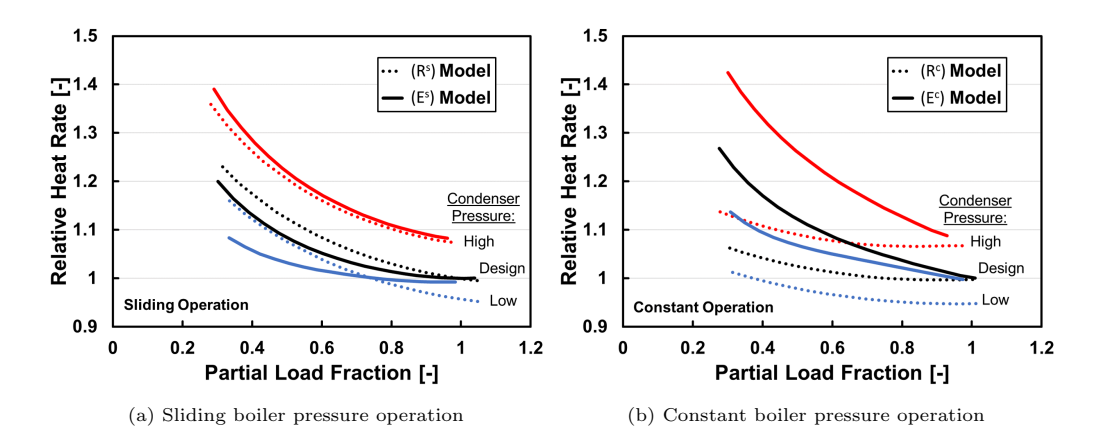


Figure 10: Comparison of the predicted relative heat rate curves for (R) and (E) as a function of partial load fraction, using (a) sliding:  $(R^s)$  and  $(E^s)$ , and (b) constant:  $(R^c)$  and  $(E^c)$  boiler pressure operation for high, design, and low condenser pressures.

## 4. Results

The dispatch optimization model is written in the AMPL modeling language version 20210630 [29] and solved using CPLEX version 12.8 [30]. Hardware architecture to generate solutions consists of a SuperServer 1028GR-TR server with an Intel Xeon E5-2620 v4s at 2.1 GHz, running Ubuntu 16.04 with 128 GB of RAM,  $1\times250$  GB SSD, and  $3\times500$  GB SSDs hard drives.

## 4.1. Cycle Performance Comparison Between (R) and (E)

Figure 10 depicts a comparison of the relative heat rate curves of (R) and (E) as a function of partial load fraction, using sliding (Figure 10a) and constant (Figure 10b) boiler pressure operation for high, design, and low condenser pressures. We evaluate the relative heat rate relationships of (R) and (E) using design molten salt inlet temperature, values of normalized molten salt mass flow rates between 0.3 and 1.05, and constant condenser pressures of 0.2, 0.08, and 0.036 bar, corresponding to high, design, and low condenser pressure, respectively. For (R), we employ the look-up performance tables, used by SAM for sliding and constant pressure operation, to evaluate its relative heat rate curves for the given condenser pressures [21].

Figure 10a shows that  $(R^s)$  and  $(E^s)$  are in close agreement with each other in both magnitude and rate-of-change at high and design condenser pressures. The differences between the relative heat rates of  $(R^s)$  and  $(E^s)$  diverge for the low condenser pressures which, at a partial load fraction of about 0.3, renders the relative heat rate of  $(R^s)$  0.12 greater than that of  $(E^s)$ . In addition, as partial load fraction increases to 1, the relative heat rate curve of  $(E^s)$  at low condenser pressure converges to design values, wheres that of  $(R^s)$  continues to decrease to a value below 1. The described behavior observed from our model,  $(E^s)$ , is due to choked flow limits at the LPT exit, resulting in a decrease in enthalpy drop across the LPT and an increase in exhaust losses; see Spencer et al. [4] for more details. At design condenser pressure,  $(R^s)$  provides a more conservative relative heat rate curve compared to  $(E^s)$ . However, the relative heat rate of  $(R^s)$  at low

condenser pressure either overpredicts cycle performance, when partial load fraction is greater than 0.75, or underpredicts cycle performance compared to  $(E^s)$ .

Figure 10b shows that  $(R^c)$  and  $(E^c)$  are in agreement at full-load condition; that is, partial load fraction equals 1 at high and design condenser pressures. However,  $(R^c)$  and  $(E^c)$  diverge significantly as partial load fraction is reduced and at low condenser pressures.  $(R^c)$  estimates a better (lower) relative heat rate curve compared to  $(R^s)$ . Sliding operation results in higher cycle efficiencies compared to constant operation, as expected based on the descriptions of the two operating strategies in Section 1. Therefore, we conclude that the  $(R^c)$  relative heat rate curve estimates are an unrealistically optimistic representation of cycle performance at part-load operations. While sliding and constant boiler pressure operation are both available within SAM, the default is constant pressure, consistent with that in  $(R^c)$ .

## 4.2. Impact on Annual Performance for a CSP-only System

We first simulate annual performance for a CSP-only system (that is, without hybridized photovoltaics) using each of the five power cycle models previously discussed - (C), (R<sup>s</sup>), (E<sup>s</sup>), (R<sup>c</sup>), and (E<sup>c</sup>). The simulations consider all possible design configurations, and optimize dispatch according to the characteristics of each cycle. Next, we select for further analysis the CSP-only design corresponding to the lowest power purchase agreement (PPA) price. In this case, the design includes a solar multiple of 2.5 and 10 hours of TES.

Power purchase agreement price is a financial metric that accounts for both the amount of energy the system produces and the time at which production occurs, through the use of time-of-delivery factors. This metric represents the price at which a project can sell electricity to achieve the project's internal rate of return at the end of the desired horizon, and is calculated using SAM's financial models [15] with a default target internal rate of return of 11 % occurring in year 20 of the project with a 1 % PPA price escalation per year [31, 32].

Figure 11 depicts the annual percentage of time the power cycle spends in a thermal input range for a CSP-only system using the five off-design performance cycle models. From Figure 11,  $(R^s)$ ,  $(E^s)$ , and  $(E^c)$  primarily operate at either a full-load or at an "off" state, which accounts for 35-45 % and 20-30 % of annual operation, respectively.  $(R^c)$  dispatches in a fashion similar to (C), that is, it spends more time in the low power state (90,120] than in the "off" state. (C) and  $(R^c)$  spend only about 8 % of the year in an "off" state, which is 3-4 times less than the other cycle models. The reverse is true for the low power state, in which  $(R^c)$  and (C) operate about three to six times more often in the low power state compared to the other cycle models.

Table 5 presents annual performance metrics for the five different off-design cycle models of the CSP-only system with a solar multiple of 2.5 and 10 hours of TES, and contains the following annual performance metrics: capacity factor, number of cycle starts, cycle ramp index, reliability (10 %, 25 %, and 50 %), and simulation time. We describe each of these in turn. The value " $\Delta$ " represents the percentage change between (E) and (R) utilizing the same boiler pressure operation (sliding or constant); see Equation (16).

$$\Delta = \frac{(\mathsf{E}^{s/c}) - (\mathsf{R}^{s/c})}{(\mathsf{R}^{s/c})} * 100 \tag{16}$$

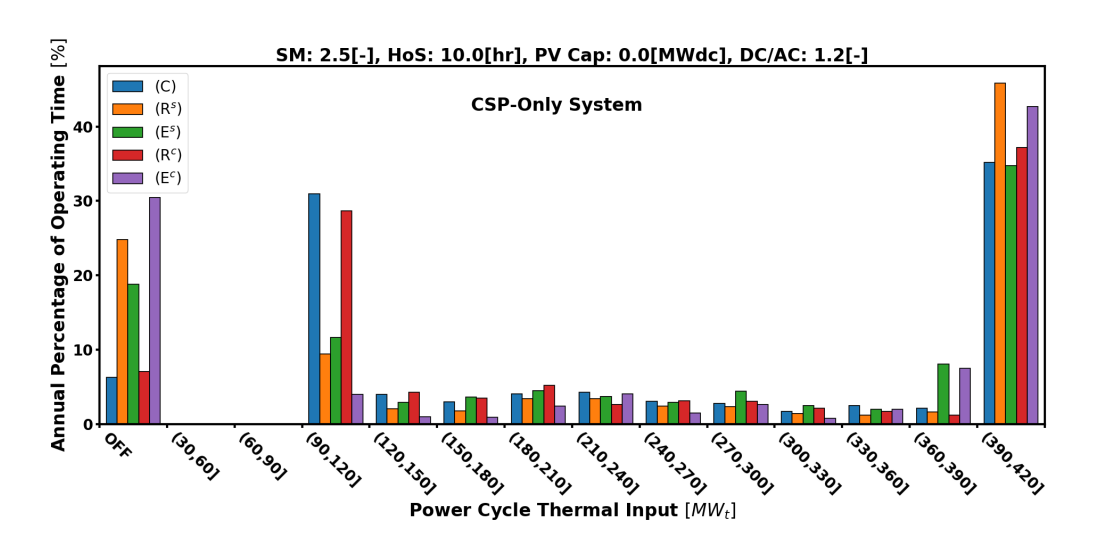


Figure 11: Annual percentage of time the power cycle spends in a thermal input range for a CSP-only system using the five off-design performance cycle models. The [0,30] range only contains values of 0 MW<sub>t</sub> thermal input, corresponding to the cycle being in an "off" state. [solar multiple (SM), hours of storage (HoS), photovoltaic field capacity (PV Cap), DC-to-AC ratio (DC/AC)]

Table 5: Comparison between annual performance metrics using the various off-design cycle models for a CSP-only system comprised of a solar multiple of 2.5 and 10 hours of TES. Annual performance metrics shown are: capacity factor, number of cycle starts, cycle ramp index, reliability (10 %, 25 %, and 50 %), and simulation time. The value " $\Delta$ " represents the percentage change between (E) and (R) utilizing the same boiler pressure operation (sliding or constant).

	Capacity	Cycle	Cycle	Reliability			Simulation
$\mathbf{Cycle}$	Factor	Starts	Ramp	10 %	25 %	50~%	Time
$\mathbf{Model}$	[%]	[-]	[%]	[%]	[%]	[%]	[min.]
(C)	55.80	57	68.5	94.85	90.93	83.25	8.53
$(R^s)$	56.33	139	97.6	96.48	93.47	88.61	14.27
$(E^s)$	58.15	88	91.3	97.02	93.68	84.32	13.47
$\Delta$ [%]	+3.23	-36.69	-6.45	+0.56	+0.22	-4.84	-5.61
$(R^c)$	56.93	46	90.8	95.53	91.91	81.92	9.35
$(E^c)$	57.72	204	92.1	97.28	93.85	89.15	17.50
$\Delta$ [%]	+1.39	+343.48	+1.43	+1.83	+2.11	+8.83	+87.17

Capacity factor is the ratio of annual energy generation and the maximum possible energy generation, which is calculated using a grid transmission limit of  $165~\mathrm{MW}_e$  as the maximum system output; see Equation (17). Due to a constant solar field design and solar resource, the five cases result in the same solar energy collection. Therefore, the capacity factor in Table 5 provides a direct comparison of solar-to-electric conversion. Table 5 shows that both (R) and (E) result in a higher capacity factor than (C) because (R) and (E) yield higher cycle efficiencies than does (C) at ambient temperatures below design conditions. CSP power cycles are typically designed for the 95 % highest ambient temperatures of the location to ensure that they can meet their rated power during high ambient temperature conditions. As a result, their full-load performance increases during

lower-than-design ambient temperatures. For sliding pressure operation,  $(\mathsf{E}^s)$  results in a higher capacity factor than  $(\mathsf{R}^s)$  due to the performance of  $(\mathsf{E}^s)$  at low ambient temperature compared to that of  $(\mathsf{R}^s)$ , shown in Figure 10a. For constant pressure operation, the difference between the capacity factors of  $(\mathsf{R}^c)$  and  $(\mathsf{E}^c)$  is smaller and is a result of more frequent operation for  $(\mathsf{R}^c)$  at low power output to avoid cycle start-ups, shown in Figure 11.

Capacity Factor = 
$$\frac{\text{Net Annual Energy } [MWh/yr]}{\text{System Transmission Limit } [MW] \times 8,760 \ [hr/yr]}$$
(17)

Cycle starts represents the number of start-up operations the power cycle undergoes throughout the year, regardless of whether the start up is "cold," "warm," or "hot" (where most of the cycle starts would be considered "hot" or "warm"). The Cycle ramp index corresponds to the average percentage of rated power ramp per day, for example, 100 % represents a cycle that goes from a no generation state, to full power, and back to no generation every day; see Equation (18). For sliding pressure operation,  $(E^s)$  results in a 37 % reduction in cycle starts compared to  $(R^s)$ . This behavior is due to the lower relative heat rate of  $(E^s)$  compared to that of  $(R^s)$  at low condenser pressure and low partial load fraction (shown in Figure 10a). (R<sup>c</sup>) results in the lowest number of cycle starts, while  $(E^c)$  results in the highest, which is 343 % more than  $(R^c)$ . This difference is due to under-accounting in  $(R^c)$  of performance degradation at lower power output (shown in Figure 10b), which results in behavior similar to that of (C), that is, a low number of cycle starts. Sliding pressure operation results in higher partial load cycle efficiency compared to constant pressure. As a result,  $(E^s)$  operates more frequently at low load than does (E<sup>c</sup>), which reduces the number of cycle starts by about a factor of two.

Cycle Ramp Index = 
$$\frac{\sum_{t=1}^{8,760} |\dot{W}_t - \dot{W}_{t-1}|}{2 \cdot \dot{W}^{cycle}} \cdot 100$$
 (18)

Reliability at x % is defined as the system's capacity factor for the x % highest-valued time periods; see Equation (19). For example, during the year's 10 % highest-valued hours (876 hours), (C) generates 94.85 % of the maximum possible energy, that is, the product of the grid transmission limit of 165 MW<sub>e</sub> and the number of high-valued time periods. Reliability at several different thresholds yields insight on how the system configuration is able to provide power during high-value time periods. (R<sup>s</sup>) and (E<sup>s</sup>) result in similar 10 % and 25 % reliabilities, but differ in 50 % reliability because (E<sup>s</sup>) avoids cycle starts by operating at partial load more often than does (R<sup>s</sup>); this behavior is a result of the lower partial load heat rate in (E<sup>s</sup>) compared to (R<sup>s</sup>). Table 5 shows that (E<sup>c</sup>) results in higher 10 %, 25 %, and 50 % reliabilities compared to (R<sup>c</sup>), because: (i) the cycle performance of (E<sup>c</sup>) is slightly higher than that of (R<sup>c</sup>) at full-load operation; and (ii) (R<sup>c</sup>) operates at low load more often than does (E<sup>c</sup>) to avoid cycle starts, but at the cost of forgoing high-valued time periods.

Reliability at 
$$x \% = \frac{\sum_{t \in \hat{\mathcal{T}}_x} \dot{W}_t^{net}}{\dot{W}_t^{max} |\hat{\mathcal{T}}_x|}$$
 (19)

Simulation time is the wall clock time between when the simulation starts and ends, and includes the time to design the heliostat field and simulate the power cycle using

dispatch optimization and updating the simulation schedule every day [17]. Table 5 provides simulation times for all the cycle models, and shows that the computational expense required for (C) and ( $R^c$ ) is about 70 % less than for the others because of the more pronounced trade-offs between cycle start-up and low load operation in the dispatch optimization runs.

## 4.3. Impact on Annual Performance for a CSP-PV Hybrid System

635

To investigate cycle dispatch behavior for a CSP-PV hybrid system, we select a hybrid design that corresponds to the lowest PPA price across all cycle models, that is, a CSP system with a solar multiple of 1.25, 8 hours of TES, and a 225  $\rm MW_{DC}$  PV system with a 1.3 DC-to-AC ratio. However, the hybrid system configuration corresponding to "lowest PPA" design varies depending on the cycle model implemented (see §4.4).

The histogram in Figure 12 depicts the annual percentage of time that the power cycle spends in a thermal input range for a CSP-PV hybrid system using the five off-design performance cycle models, and shows that the system exhibits a large decrease in full power operation as a result of the solar multiple being half that of the CSP-only design (compare with Figure 11). Over the year, the power cycle is in an "off" state a majority of the time (approximately 40 to 63 %). As a result, the power cycle operates at full load for 10 to 18 % of the year, compared to the 35 to 46 % seen in the CSP-only case. Like the CSP-only case, (C) and ( $\mathbb{R}^c$ ) favor low power output over cycle shutdown and start-up because they are overly optimistic regarding part-load efficiency performance.

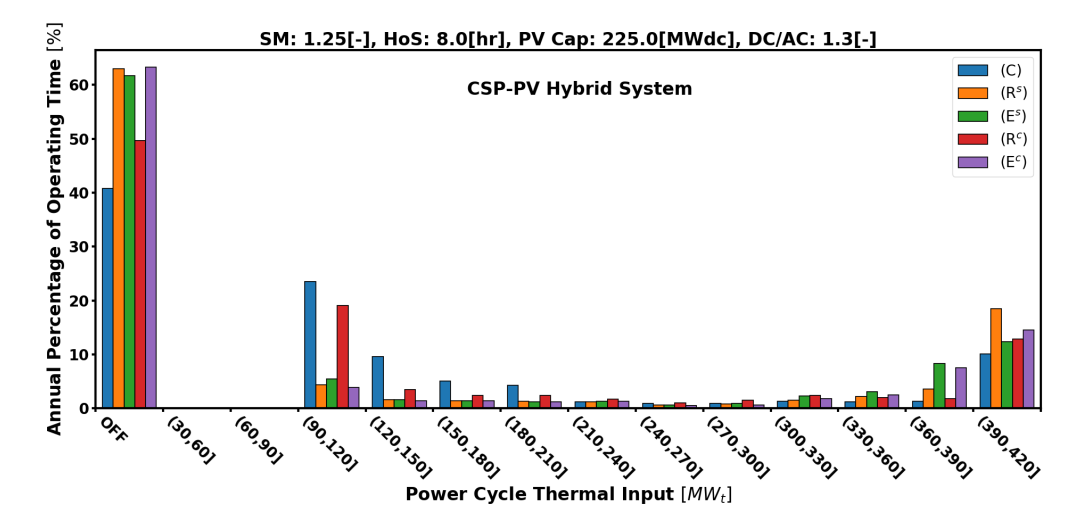


Figure 12: Annual percentage of time the power cycle spends in a thermal input range for a CSP-PV hybrid system using the five off-design performance cycle models. The [0,30] range only contains values of  $0~\mathrm{MW}_t$  thermal input, corresponding to the cycle being in an "off" state. [solar multiple (SM), hours of storage (HoS), photovoltaic field capacity (PV Cap), DC-to-AC ratio (DC/AC)]

Table 6 presents annual performance metrics for the five different off-design cycle performance models of the CSP-PV hybrid system with lowest PPA price design. In addition to the annual performance metrics presented in Table 5 for the CSP-only system, Table 6 contains the percentage of CSP and PV curtailment.

Table 6: Comparison between annual performance metrics using the various off-design cycle models for a CSP-PV hybrid system comprised of a solar multiple of 1.25, 8 hours of TES, and 225 MW<sub>DC</sub> PV system with a DC-to-AC ratio of 1.3. Annual performance metrics shown are: capacity factor, number of cycle starts, cycle ramp index, percentage of CSP curtailment, percentage of PV curtailment, reliability (10 %, 25 %, and 50 %), and simulation time. We also report " $\Delta$ ," which represents the percentage change between (E) and (R) utilizing the same boiler pressure operation (sliding or constant).

	Capacity	Cycle	Cycle	Curtai	lment	1	Reliability	У	Simulation
Cycle	Factor	Starts	Ramp	CSP	PV	10%	25%	50%	Time
Model	[%]	[-]	[%]	[%]	[%]	[%]	[%]	[%]	[min.]
(C)	61.07	289	84.86	0.69	3.73	97.25	91.07	90.07	13.19
(R <sup>S</sup> )	62.46	337	98.25	1.30	1.52	97.79	94.24	92.17	16.86
(E <sup>s</sup> )	63.20	330	98.76	1.21	1.77	98.15	94.51	92.16	17.47
Δ [%]	+1.18	-2.08	+0.52	-6.92	+16.45	+0.37	+0.29	-0.01	+3.62
(R <sup>c</sup> )	61.91	288	98.57	0.68	3.34	97.26	92.19	90.89	14.24
$(E^c)$	62.89	340	99.08	2.04	1.24	98.01	94.59	92.07	16.92
$\Delta$ [%]	+1.58	+18.06	+0.52	+200.00	-62.87	+0.77	+2.60	+1.30	+18.82

Table 6 shows that cycle models (C) and ( $R^c$ ) perform similarly across all metrics; likewise, there are small differences between cycle models ( $R^s$ ), ( $E^s$ ), and ( $E^c$ ). (C) and ( $R^c$ ) result in fewer cycle starts than the other models because their cycles operate at part-load more frequently due to the improper degradation of performance at partial load outweighing the cost of a start-up event. Across all cycle models, hybridization of PV with CSP results in at least a 170 % increase in the number of starts compared to the CSP-only design. The (C) and ( $R^c$ ) models exhibit more PV curtailment, about 3.5 % of the annual PV generation, than CSP curtailment, about 0.7 % of the annual CSP generation; this is because (C) and ( $R^c$ ) more frequently operate at the minimum turn down limit during days when the grid constraint is tight, resulting in PV curtailment and fewer cycle starts. With the other cycle models, this trade-off yields in a cycle shutdown during the solar hours, forcing thermal energy storage to reach capacity before the solar day ends, i.e., CSP curtailment. Table 6 shows that (C) and ( $R^c$ ) possess lower reliabilities and simulation times compared to the other models.

## 4.4. Implications on System Design

To investigate the effect that off-design cycle performance has on system design, we determine the system design corresponding to the lowest PPA price for each level of PV system DC capacity, shown in Table 7, which presents the solar multiple and hours of storage corresponding to the lowest PPA price design for two groups of off-design performance cycle models, categorized by agreement in the design characteristics of solar multiple and hours of storage. The first group consists of (C) and ( $\mathbb{R}^c$ ), while the second group consists of ( $\mathbb{R}^s$ ), ( $\mathbb{E}^s$ ), and ( $\mathbb{E}^c$ ). Table 7 shows that system design parameter DC-to-AC ratio has more variation between the cycle models.

Table 7 demonstrates that the two groups result in the same solar multiple and hours of storage for a PV system DC capacity of 0, 25, 125, 175, and 200  $MW_{DC}$ , leading us to conclude that off-design performance has less impact on the lowest PPA design's solar multiple and hours of storage combination when the capacity of the PV system is smaller. The discrepancy between the resulting lowest PPA design configurations for off-design cycle models leads to different "optimal" system designs.

We investigate, for the designs in Table 7 corresponding to the lowest-PPA-priced systems, their resulting annual simulation metrics as a function of: (i) PV system DC capacity, and (ii) the particular cycle performance model. Figure 13 depicts normalized PPA, capacity factor, annual cycle starts, and top 25 % reliability for the five power

Table 7: Solar multiples, hours of storage, and DC-to-AC ratios corresponding to the lowest PPA price for each DC capacity of the PV system. Model group 1 includes models  $\{(C), (R^c)\}$ ; Model group 2 includes  $\{(R^s), (E^s), (E^c)\}$ .

PV Cap.	Solar Multiple		Hours of Storage		DC-to-AC Ratio				
$MW_{DC}$	Group 1	Group 2	Group 1	Group 2	(C)	(R <sup>c</sup> )	(R <sup>S</sup> )	(E <sup>s</sup> )	(E <sup>c</sup> )
0	2.50	2.50	10	10			N/A		
25	2.50	2.50	10	10	1.3	1.1	1.2	1.1	1.0
50	2.50	2.50	10	12	1.1	1.2	1.3	1.2	1.2
75	2.25	2.50	10	12	1.1	1.2	1.2	1.2	1.1
100	2.25	2.50	12	12	1.2	1.0	1.1	1.2	1.2
125	2.25	2.25	12	12	1.2	1.2	1.2	1.3	1.2
150	2.00	2.25	12	12	1.2	1.2	1.3	1.3	1.3
175	2.00	2.00	12	12	1.3	1.3	1.3	1.3	1.2
200	2.00	2.00	12	12	1.3	1.3	1.3	1.2	1.3
225	0.75	1.25	6	8	1.3	1.2	1.3	1.3	1.3

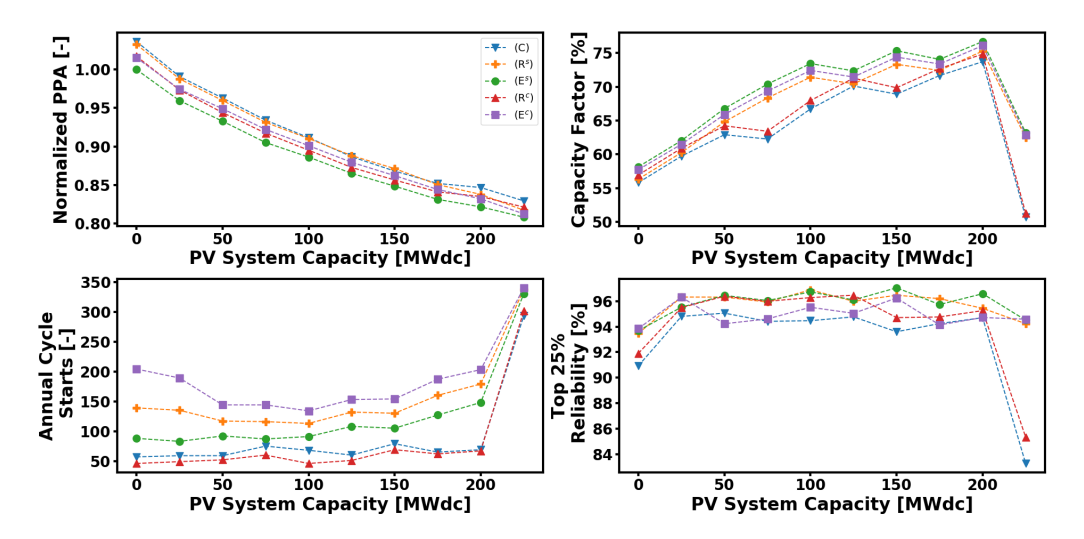


Figure 13: Normalized PPA, capacity factor, annual cycle starts, and top 25% reliability for the five power cycle models at varying DC capacity of the PV system. Design for each data point corresponds to lowest PPA price system.

cycle models. PPA prices are calculated using SAM's default costs (Version 2018.11.11) and are normalized using the lowest PPA price for the CSP-only case, which corresponds to  $107.21 \text{ /MWh}_e$  using the (E<sup>s</sup>) cycle model. For reference, the average commercial prices of electricity in California and Nevada are about  $154 \text{ /MWh}_e$  and  $77 \text{ /MWh}_e$ , respectively [33].

Figure 13 shows that PPA prices decrease as DC capacity of the PV system increases, with about a 17 % decrease from 0  $\rm MW_{DC}$  to 225  $\rm MW_{DC}$ . At any given PV system capacity, the variability in PPA price across the five off-design cycle models is small, with a maximum range of 3.5 % occurring under a 0  $\rm MW_{DC}$  PV system condition. System capacity factor depends greatly on design variable values. At a PV system DC capacity of 225  $\rm MW_{DC}$ , there is a drop in capacity factor due to the large reduction in solar multiple and hours of storage (Table 7). This result occurs because the PV system capacity is approaching the grid transmission capacity, resulting in the CSP system being shut down during PV generation to reduce curtailment. Correspondingly, for all the off-design cycle models, there is a steep increase in the number of starts as the PV system's DC capacity approaches 225  $\rm MW_{DC}$  because the grid transmission capacity constraint

requires the cycle to shut down during high-PV-generation time periods to mitigate PV system curtailment. Of the four metrics shown in Figure 13, annual cycle starts has the greatest variability between the different power cycle models. Reliability for the 25 % highest-valued time periods is relatively constant for the five power cycle models, except for (C) and ( $\mathbb{R}^c$ ) at high PV system DC capacity.

## 5. Conclusions

We present a methodology to model a Rankine cycle with the fidelity to estimate off-design performance. We implement said methodology into Engineering Equation Solver and validate the results against data provided by our industry partners and a model from literature that implements similar methodology. Then, we integrate the validated model results into SAM utilizing the "user-defined" cycle option which enables us to investigate the impact of off-design cycle performance on cycle operation, overall CSP plant performance, and minimum PPA price system design. The primary contribution of our work lies in investigating and understanding the Rankine cycle off-design performance impact on optimized dispatch decisions and the propagation of those decisions into a CSP system's design, annual performance, and economics.

The results indicate that previous modeling of Rankine cycle off-design performance is either too optimistic (constant boiler pressure) or conservative (sliding boiler pressure). The former causes unrealistic operation of the power cycle, such as an increased frequency of partial load operation to avoid cycle starts, which can lead to sub-optimal system designs. The latter results in lower solar-to-electric conversion, which negatively impacts plant finances and PPA price. Future work will update SAM's default Rankine cycle models using estimates from (E) of off-design performance and will investigate power cycle transients at increasing time fidelity.

## 6. Appendix

Acronyms

Table 8: Units, acronyms, model names and notation.

Units	D 1'	
$^{\circ}\mathrm{C}$	Degrees celsius	
$\operatorname{hr}$	Hour	
K	Kelvin	
kg	Kilograms	
kJ	Kilojoules	
kPa	Kilopascals	
kW	Kilowatts	
MW	Megawatts	
$MW_e$	Megawatts electric	
$MW_t$	Megawatts thermal	
MWh	Megawatt hours	
S	Seconds	

27

CSP	Concentrated solar power
EES	Engineering Equation Solver
HPT	High-pressure turbine
IAPWS	International Association for the Properties of Water and Steam
$\operatorname{IPT}$	Intermediate-pressure turbine
$_{ m LPT}$	Low-pressure turbine
MILP	Mixed integer linear program
NTU	Number of transfer units
PPA	Power purchase agreement
PV	Photovoltaics
SAM	System Advisory Model
SCC	Spencer-Cotton-Cannon Method
SM	Solar multiple
TES	Thermal energy storage
Models	
(C)	Constant efficiency model
(D)	Data provided by our industry partner
(E)	Rankine cycle model capable of off-design performance calculations using EES
$(E^c)$	Off-design performance cycle model (E) pertaining to constant boiler pressure operation
$(E^s)$	Off-design performance cycle model (E) pertaining to sliding boiler pressure operation
(R)	SAM's Rankine performance model
$(R^c)$	Off-design performance cycle model (R) pertaining to constant boiler pressure operation
$(R^s)$	Off-design performance cycle model (R) pertaining to sliding boiler pressure operation
Notation	a: Entire Parameters
$a_0, a_1, a_2$	Coefficients for the constant, linear and quadratic terms, respectively,
	on the expansion curve $[kJ/kg-K]$ , $[1/K]$ , $[kg/kJ-K]$
$a_{ij}$	Coefficient for the $(i, j)$ exponent pair (see Table 1) [-]
c	Specific heat [kJ/kg-K]
f	Fraction [-]
h	Specific enthalpy [kJ/kg]
HR	Heat rate [-]
$\overline{HR}$	Relative heat rate [-]
ITD	Initial temperature difference [K]
k	Proportionality constant [1/kg-m]
$\dot{m}$	Mass flow rate [kg/s]
n	Number of [-]
P	Pressure [kPa]
$ ilde{P}_c$	Normalized condenser pressure [-]
â	The state of the s

Normalized heat rejection [-] Rate of heat transfer [kW]

Specific entropy [kJ/kg-K]

Temperature [°C]

Ideal gas constant for air [kJ/kg-K]

 $\hat{Q}$   $\hat{Q}$   $\hat{Q}$  R

$\hat{T}$	Normalized temperature [-]
$\hat{\mathcal{T}}_x$	Subset of time periods which contains the $x$ % of the highest-valued period [-]
$\dot{W}$	Power [kW]
$\dot{W}^{cycle}$	Cycle power [kW]
$\beta$	Shape factor parameter [-]
$\Delta$	Difference (between two quantities) $[\cdot]$
$\eta$	Efficiency [-]
ho	Density $[kg/m^3]$
UA	Overall heat transfer coefficient [kW/m²-K]

# Notation: Subscripts and Superscripts

TTOTATION	. Subscripts and Superscripts
AC	Alternating current
acc	Air-cooled condenser
air	Air
amb	Ambient
c	Cold fluid of the heat exchanger
D	Design condition
db	Dry bulb
DC	Direct current
e	Extraction (turbine)
fan	Fan
g	Gross electric
h	Hot fluid of the heat exchanger
i	Stage inlet
m	Mechanical
max	Maximum
min	Minimum
net	Net
0	Stage outlet
p	Pump
PL	Part-load
rej	Rejection
s	Isentropic
sat	Saturated
t	Thermal

# **Notation: Functions**

$C_p(\cdot)$	EES's specific heat function
$P_{sat}(\cdot)$	EES's saturation pressure function
$s(\cdot), s'(\cdot)$	LPT expansion curve of entropy as a second-order polynomial of enthalpy

# Acknowledgments

This work was funded by the United States Department of Energy – Energy Efficiency and Renewable Energy under award numbers DE-EE00025831 and DE-EE00030338.

#### 730 References

750

770

- Concentrating solar power projects, 2020 (accessed February 29, 2020). URL https://solarpaces.nrel.gov/.
- [2] Paul Denholm and Mark Mehos. Enabling greater penetration of solar power via the use of CSP with thermal energy storage. NREL/TP, Golden, CO, 2011.
- [3] K. C. Cotton. Evaluating and Improving Steam Turbine Performance. Cotton Fact Inc., Rexford, NY, USA, 1993.
  - [4] R. C. Spencer, K. C. Cotton, and C. N. Cannon. A Method for Predicting the Peformance of Steam Turbine-Generators...(16,500 kW and Larger). *Journal of Engineering for Power*, 85:249–298, October 1963.
- [5] David H. Cooke. Modeling of Off-Design Multistage Turbine Pressures by Stodola's Ellipse. Technical report, Richmond, Virginia, November 1983.
  - [6] David H. Cooke. On Prediction of Off-Design Multistage Turbine Pressures by Stodola's Ellipse. Journal of Engineering for Gas Turbines and Power, 107(7):596–606, 1985.
  - [7] Nico Woudstra, Theo Woudstra, Armando Pirone, and Teus van der Stelt. Thermodynamic evaluation of combined cycle plants. Energy Conversion and Management, 51(5):1099-1110, May 2010.
  - [8] R. Chacartegui, D. Sánchez, J. A. Becerra, A. Muñoz, and T. Sánchez. Performance Analysis of a 565 MW Steam Power Plant. In *Volume 7: Turbomachinery, Parts A, B, and C*, pages 2427–2436, Vancouver, British Columbia, Canada, 2011. ASME.
- [9] Carolina Marugán-Cruz, D. Serrano, J. Gómez-Hernández, and S. Sánchez-Delgado. Solar multiple optimization of a DSG linear Fresnel power plant. Energy Conversion and Management, 184: 571–580. March 2019.
  - [10] Joshua D. McTigue, Jose Castro, Greg Mungas, Nick Kramer, John King, Craig Turchi, and Guangdong Zhu. Hybridizing a geothermal power plant with concentrating solar power and thermal storage to increase power generation and dispatchability. Applied Energy, 228:1837–1852, October 2018.
- 755 [11] Philip G. Brodrick, Adam R. Brandt, and Louis J. Durlofsky. Operational optimization of an integrated solar combined cycle under practical time-dependent constraints. *Energy*, 141:1569– 1584, December 2017.
  - [12] E. D. Castronuovo and J. A. P. Lopes. On the optimization of the daily operation of a wind-hydro power plant. IEEE Transactions on Power Systems, 19(3):1599–1606, August 2004.
- [13] Aldo Bischi, Leonardo Taccari, Emanuele Martelli, Edoardo Amaldi, Giampaolo Manzolini, Paolo Silva, Stefano Campanari, and Ennio Macchi. A detailed MILP optimization model for combined cooling, heat and power system operation planning. *Energy*, 74:12–26, September 2014.
  - [14] Zhe Zhou, Pei Liu, Zheng Li, Efstratios N. Pistikopoulos, and Michael C. Georgiadis. Impacts of equipment off-design characteristics on the optimal design and operation of combined cooling, heating and power systems. Computers & Chemical Engineering, 48:40–47, January 2013.
  - [15] Nathan J. Blair, Nicholas A. DiOrio, Janine M. Freeman, Paul Gilman, Steven Janzou, Ty W. Neises, and Michael J. Wagner. System Advisor Model (SAM) General Description (Version 2017.9.5). Technical Report NREL/TP-6A20-70414, 1440404, May .
  - [16] Michael J Wagner. Simulation and Predictive Performance Modeling of Utility-Scale Central Receiver System Power Plants. Master of Science, University of Wisconsin Madison, 2008.
  - [17] Michael J Wagner, Alexandra M Newman, William T Hamilton, and Robert J Braun. Optimized dispatch in a first-principles concentrating solar power production model. Applied Energy, 203: 959–971, 2017.
- [18] Michael J. Wagner, William T. Hamilton, Alexandra Newman, Jolyon Dent, Charles Diep, and Robert Braun. Optimizing dispatch for a concentrated solar power tower. Solar Energy, 174: 1198–1211, November 2018.
  - [19] William T. Hamilton, Mark A. Husted, Alexandra M. Newman, Robert J. Braun, and Michael J. Wagner. Dispatch optimization of concentrating solar power with utility-scale photovoltaics. *Optimization and Engineering*, 21:335–369, September 2020.
- [20] S.A. Klein. Engineering Equation Solver (EES) Academic Professional V10.452-3D. F-Chart Software, July 2018 (accessed February 29, 2020). URL http://fchart.com/ees/eeshelp/eeshelp.
  - [21] National Renewable Energy Laboratory. SAM Simulation Core (SSC). https://github.com/NREL/ssc/blob/develop/tcs/csp\_solver\_pc\_Rankine\_indirect\_224.cpp, 2019 (accessed May 20, 2019).
- [22] F. Lippke. Simulation of the part-load behavior of a 30 MWe SEGS plant. Technical Report SAND-95-1293, Sandia National Labs., Albuquerque, NM (United States), June 1995 (accessed February 29, 2020). URL https://www.osti.gov/biblio/95571.

- [23] Theodore L. Bergman, Adrienne S. Lavine, Frank P. Incropera, and David P. Dewitt. Fundamentals of Heat and Mass Transfer. John Wiley & Sons, Inc., 7 edition, 2011.
- [24] Angela M. Patnode. Simulation and Performance Evaluation of Parabolic Trough Solar Power Plants. Master of Science, University of Wisconsin - Madison, Wisconsin, 2006.
  - [25] A. B. Zavoico. Solar power tower design basis document. Technical Report SAND2001-2100, Sandia National Laboratories, Albuquerque, NM (United States).
- [26] Félix Ignacio Pérez Cicala. Modelling of Rankine cycles using Spencer, Cotton and Cannon. https://www.github.com/FelixPerezCicala/modRankineSCC, 2019 (accessed February 29, 2020).
- [27] National Renewable Energy Laboratory. System Advisor Model (SAM) Version 2018.11.11, May 2019. URL https://sam.nrel.gov/images/web\_page\_files/sam-help-2018-11-11-r4.pdf.
- [28] Michael J. Wagner and Tim Wendelin. SolarPILOT: A power tower solar field layout and characterization tool. Solar Energy, 171:185–196, September 2018.
- [29] AMPL. AMPL Version 10.6.16. AMPL Optimization LLC, 2009.
  - [30] IBM. IBM ILOG CPLEX Optimization Studio: CPLEX User's Manual, 2016.
  - [31] W. Short, D.J. Packey, and T. Holt. A manual for the economic evaluation of energy efficiency and renewable energy technologies. Technical Report NREL/TP-462-5173, 35391, 1995.
  - [32] System Advisor Model (SAM), 2020 (accessed March 20, 2020). URL https://sam.nrel.gov/.
- [33] Electric power monthly, 2020 (accessed April 4, 2020). URL https://www.eia.gov/electricity/monthly.